coatings

MDPI

Article

Optimization of Friction Stir Processing Parameters for Improvement of Mechanical Properties of AlSi7Mg0.2 Alloy

Mahmoud A. Alzahrani [1], Ghazi Alsoruji [1], Essam B. Moustafa [1], Ahmed O. Mosleh [2,*] and Samah S. Mohamed [2]

[1] Mechanical Engineering Department, Faculty of Engineering, King Abdulaziz University, Jeddah 21589, Saudi Arabia; alzahrani@kau.edu.sa (M.A.A.); gsaati@kau.edu.sa (G.A.); abmostafa@kau.edu.sa (E.B.M.)

[2] Mechanical Engineering Department, Faculty of Engineering at Shoubra, Benha University, Cairo 11629, Egypt; samah.samir@feng.bu.edu.eg

* Correspondence: ahmed.omar@feng.bu.edu.eg

Abstract: This paper investigates the effects of Friction Stir Processing (FSP) parameters on the microstructure and mechanical properties of an Al-Si7Mg0.2 alloy. The study's findings indicate that augmenting the rotational velocity of the tool in the context of Friction Stir Processing can reduce grain size and enhance the alloy's mechanical properties. The optimization of process temperature plays a vital role in managing the thermal profile and preventing undesirable consequences such as overheating or excessive cooling. These adverse effects can significantly impact the microstructure and properties of the alloy. The finer grain size of the FSPed samples resulted from the intense plastic deformation and dynamic recrystallization during the process. This grain refinement improved hardness, wear, and corrosion resistance. The temperature distribution during FSP using finite element simulation was highly dependent on the process parameters, such as the rotational speed and the dwell time. The results of this study are employed to develop a fitting model to predict the temperature distribution along the workpiece during the dwelling stage, which can be used to optimize the process parameters for different applications. The optimization of the heat generation inside the stirred zone plays a vital role in managing the thermal profile and preventing undesirable consequences such as overheating or excessive cooling. These adverse effects can significantly impact the microstructure and properties of the alloy.

Keywords: Al-Si; corrosion rate; wear resistance; fiction stir processing; surface modification; numerical simulation

Citation: Alzahrani, M.A.; Alsoruji, G.; Moustafa, E.B.; Mosleh, A.O.; Mohamed, S.S. Optimization of Friction Stir Processing Parameters for Improvement of Mechanical Properties of AlSi7Mg0.2 Alloy. *Coatings* **2023**, *13*, 1667. https://doi.org/10.3390/coatings13101667

Academic Editor: Yanxin Qiao

Received: 8 August 2023
Revised: 11 September 2023
Accepted: 21 September 2023
Published: 22 September 2023

1. Introduction

Friction Stir Processing (FSP) has emerged as a solid-state technique that has attracted considerable interest in recent times owing to its potential to modify the microstructure and improve the mechanical characteristics of different alloys. One particular alloy that has been the focus of numerous investigations is the Al-Si alloy. This alloy is widely used in industries such as automotive and aerospace due to its desirable combination of strength, corrosion resistance, and lightweight properties. Friction Stir Processing has shown promising results in improving the microstructural, tribological, and corrosion behavior of the AlSi7Mg0.2 alloy. The microstructural modification achieved through Friction Stir Processing is a key factor in enhancing the alloy's mechanical properties and corrosion resistance. By subjecting the alloy to severe plastic deformation, FSP promotes grain refinement and homogenization of the microstructure [1–4]. Implementing Friction Stir Processing on cast aluminum and magnesium alloys led to the fragmentation of large dendrites and secondary phases and the reduction in the size of matrix grains, dissolution of precipitates, and removal of porosity. As a result, the mechanical characteristics of the castings were notably enhanced [5–7]. The frictional heat generated by the tool causes the material to deform, which refines the grain

size and introduces residual stresses plastically. These changes in the microstructure improve the material's strength, ductility, and fatigue resistance [8–10]. The refined microstructure contributes to better tribological performance by reducing friction and wear [11–13]. Moreover, Friction Stir Processing has been found to enhance the corrosion resistance of the AlSi10Mg alloy by creating a more compact and less corrosion-susceptible microstructure [14,15]. Various studies have consistently observed the improvement in mechanical properties and corrosion resistance observed in the AlSi10Mg alloy after Friction Stir Processing [16,17]. For example, a study by Szymczak et al. demonstrated that FSP significantly increased the hardness and tensile strength of the AlSi7Mg0.3 alloy. Furthermore, FSP reduces the size of secondary dendrite arm spacing (SDAS) and enhances the mechanical strength characteristics. It also resulted in a more uniform distribution of intermetallic phases and reduced porosity, which further improved the mechanical properties of the alloy [18]. In addition to the experimental investigations, simulation studies have also been conducted to understand the Friction Stir Processing and heat generation mechanisms involved in modifying the microstructure and enhancing the mechanical properties of alloys [19]. Optimizing aluminum alloy's Friction Stir Processing parameters for enhanced mechanical and tribological properties was investigated by many authors [20–24]. Taguchi's experimental design was employed to optimize the parameters of Friction Stir Processing for AA6061/SiC surface composites; the study found that the highest microhardness was obtained when using a tool rotational speed of 1400 rpm, a traverse speed of 50 mm/min, and a tilt angle of 2.5 degrees [25].

The utilization of the CEL model can serve as a robust computational instrument for emulating intricate process mechanics and enhancing the FSP process parameters in the context of industrial implementations [26]. These simulation studies aim to provide insights into the complex thermal and mechanical interactions that occur during Friction Stir Processing. They help predict temperature distribution, material flow, and microstructure evolution [27,28]. These simulation studies have confirmed that the generation of frictional heat and the stirring action play a crucial role in achieving the desired microstructural modifications. Furthermore, the simulation studies have also revealed that process parameters such as rotational speed, traverse speed, and tool geometry significantly influence the alloy's microstructural evolution and mechanical performance during Friction Stir Processing [29,30]. For instance, increased rotational speed leads to higher heat generation and more severe plastic deformation, resulting in finer grain refinement.

Furthermore, a higher traverse speed can promote better mixing of the material and prevent excessive heat accumulation, which can be detrimental to the desired microstructure modifications [31]. The research conducted on Friction Stir Processing has consistently shown that it is an effective method for improving alloys' mechanical properties and corrosion resistance [1,32]. The microstructural modifications achieved through Friction Stir Processing, such as grain refinement and homogenization, have been proven to increase various alloys' hardness and tensile strength [33,34].

Furthermore, the uniform distribution of intermetallic phases and reduced porosity achieved through Friction Stir Processing also improve mechanical properties. The implementation of Friction Stir Processing has demonstrated advantageous outcomes in terms of enhancing both hardness and wear resistance [35]. The study demonstrates that the corrosion performance of Al-Si12 alloys fabricated through selective laser melting (SLM) can be enhanced by subjecting their surfaces to Friction Stir Processing (FSP) [36]. The tool possessing a greater shoulder region facilitated increased plastic deformation on the microstructure, thereby producing a microstructure that is better suited for high-temperature deformation [37]. The rotational velocity significantly impacts the corrosion rate [38]. The microstructure of an AlSi10Mg alloy, produced through laser powder bed fusion, was modified using Friction Stir Processing to enhance its corrosion properties [39]. The optimum FSP parameters for AlSi7Mg0.2 alloy will depend on the specific application. For example, the tool rotational speed should be high enough to generate a high-temperature and high-pressure zone but not so high that the workpiece overheats. The feed rate should be high enough

to ensure the tool moves smoothly through the workpiece but not so high that the recrystallized microstructure is not fully developed. The current work aims to optimize the processing parameters to achieve multiple goals, such as minimizing grain size, wear rate, and corrosion rate. The best tool design will be the one that achieves these goals simultaneously. To achieve this, experimental work was conducted to fabricate the advanced surface. Corrosion and wear rate tests were also performed, followed by optimization and simulation modeling.

2. Materials and Methods

The present study aimed to examine the A356 (AlSi7Mg0.2) cast aluminum alloy, which possesses a chemical composition as listed in Table 1. The cast ingots, as received, were sectioned into plates of 300 × 50 × 10 mm^3 in size.

Table 1. The nominal chemical composition of the investigated alloy (wt.%).

Element	Si	Mg	Fe	Ti	Al
wt.%	7.1%	0.19%	0.1	0.09%	rest

2.1. Friction Stir Processing

The FSP procedure was conducted on a vertical CNC milling machine (Knuth-VFM5, Knuth, Wasbek, Germany). The process involved a single pass and utilized two different types of pin tools: a cylindrical pin profiled tool (CP) and a triangular pin with cylindrical corners pin tool (TP), as depicted in Figure 1. Both tools possess an identical cylindrical shoulder with a diameter of 22 mm. Figure 2 depicts the schematic representation of the processing tools along with their basic dimensions. The processing conditions and their corresponding levels are listed in Table 2.

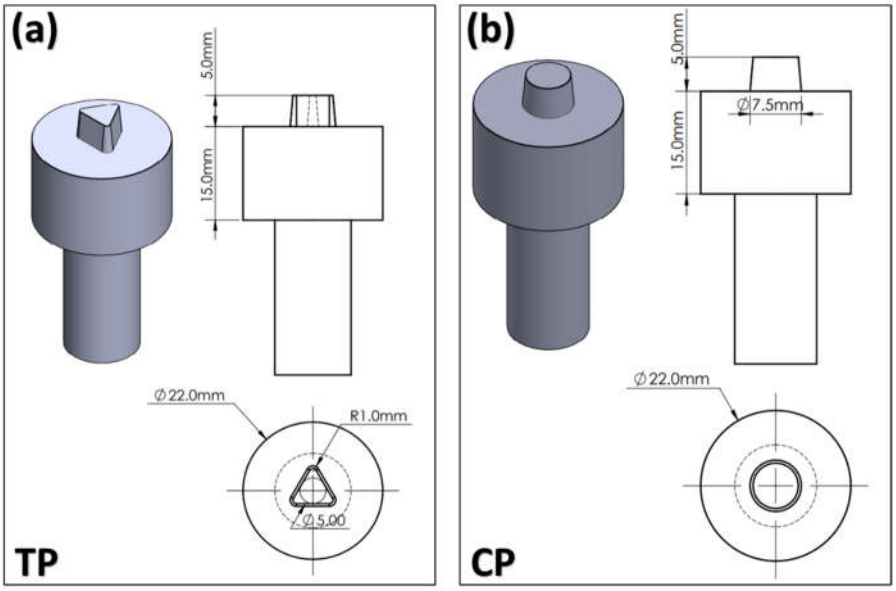

Figure 1. The used FSP tools: (**a**) triangular pin (TP) profile, (**b**) cylindrical pin, (CP) profile.

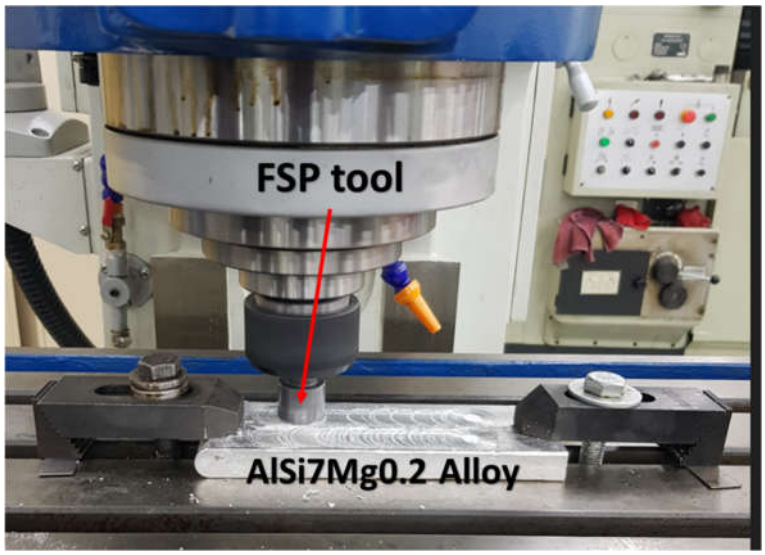

Figure 2. FS processing via an automatic milling machine.

Table 2. The levels of the Friction Stir Processing parameters used in the current work.

Processing Considerations *	Levels				
	Level 1	**Level 2**	**Level 3**	**Level 4**	**Level 5**
Tool rotational speed [rpm]	355	450	560	710	900
Traverse speed [mm/min]	10	20	40		
Tool geometry	CP	TP			

* All processed samples have a constant 2° tilt angle.

2.2. Microstructure Analysis

The specimens went through metallographic analysis following standard procedures, which involved mechanical grinding and polishing using a Struers La-boPoll5 (Struers APS, Ballerup, Denmark) polishing machine. Subsequently, the specimens were subjected to etching using Keller's reagent, which consisted of 190 mL H_2O, 5 mL HNO_3, 3 mL HCl, and 2 mL HF, for a duration ranging from 5 to 120 s at room temperature. Microstructure characterization was carried out on the samples using an optical microscope (OM) Zeiss Axiovert 200 M (Carl Zeiss, Oberkochen, Germany) and scanning electron microscope (SEM) Tescan-VEGA3 LMH (Tescan Brno s.r.o., Kohoutovice, Czech Republic). Microstructural analysis was performed using image analysis software.

2.3. Hardness Measurements

The Vickers microhardness test was performed in the stirred zone using a Zwick/Roell hardness tester (Zwick/Roell, Kennesaw, GA, USA) with a 100 g load and a 10 s shutter speed, as specified by the ASTM E-384-17 standard [40]. At least 10 measurements for each FSP condition were recorded and the hardness contours were constructed.

2.4. Wear Behavior Testes

Wear tests were conducted on the as-cast and FSPed specimens in a dry sliding condition utilizing a pin-on-ring machine tester (TNO, Delft, The Netherlands) following the ASTM G99-04A standard [41] at ambient temperature. The wear specimens possess dimensions of 10 mm × 10 mm × 10 mm. The wear tests were conducted for 20 min under a load of 50 N and at a consistent rotating speed of 100 rpm. The counter face cylinder used in the experiment had a diameter of 200 mm and was composed of 316 stainless steel. Before each

test, the cylinder was subjected to a cleaning process using acetone to eliminate any potential surface contaminants. The wear rate was calculated by measuring the weight of the specimen before and after conducting wear tests using an electronic precision balance with a resolution of ±0.1 mg, as described by Equation (1):

$$\text{wear rate } \left(\frac{\text{g}}{\text{cm}^2}\right) = \frac{\Delta \text{W}}{\text{A}} \quad (1)$$

where, ΔW is the weight loss (g), and A is the area of exposed surface to the friction (cm^2)

2.5. Corrosion Behavior Tests

The investigation of corrosion behavior was conducted by employing potentiodynamic polarization techniques on both friction-stirred zones and as-received alloys. The corrosion experiments were conducted using the workstation Autolab PGSTAT 302 N (Metrohm, Herisau, Switzerland)—a high-performance potentiostat/galvanostat instrument. The experiments were controlled using the NOVA 1.10 software (Metrohm Autolab B.V., Utrecht, The Netherlands). The NOVA software package has been specifically developed to effectively manage Autolab instruments with a USB port. The studies were conducted utilizing three typical electrode cells, including a reference Ag/AgCl electrode, a working electrode, and a platinum rod serving as a counter electrode. The specimens were submerged in a solution containing 3.5% sodium chloride (NaCl) at ambient temperature. Polarization measurements were conducted within a voltage range of −1.5 V to 1.5 V (SCE) using a scan rate of 2 mVs^{-1}. The technique of Tafel extrapolation was employed to make estimations of the resistance polarization (Rp) and the corrosion rate through the analysis of the cathodic and anodic polarization curves associated with the corresponding corrosion phenomena. Before conducting the electrochemical experiments, all exposed surfaces underwent wet polishing using emery paper with a grit size of 1200. Subsequently, the surfaces were cleaned in acetone, washed with distilled water, and dried using a dryer.

3. Results and Discussion

3.1. Microstructural Characterization

Figure 3 shows the macro-/micro-graphs of the processed sample at a rotational speed of 450 rpm and a transverse speed of 20 mm/min using the TP tool, showing the microstructure of the different regions obtained after the FSP, as an example. The processed samples exhibit typical regions obtained after both frictions stir welding or processing (Figure 3a), unaffected base metal BM (Figure 3b), heat-affected zone HAZ (Figure 3c), thermomechanical affected zone TMAZ (Figure 3c), and stirred or nugget zone SZ (Figure 3d,e). As mentioned in the materials section, the as-cast A356 alloy was processed; thus, the BM exhibits a dendritic structure of α-Al[1] as the alloy matrix, eutectic Al-Si needles[2], and separated primary Si[3] (Figure 3b).

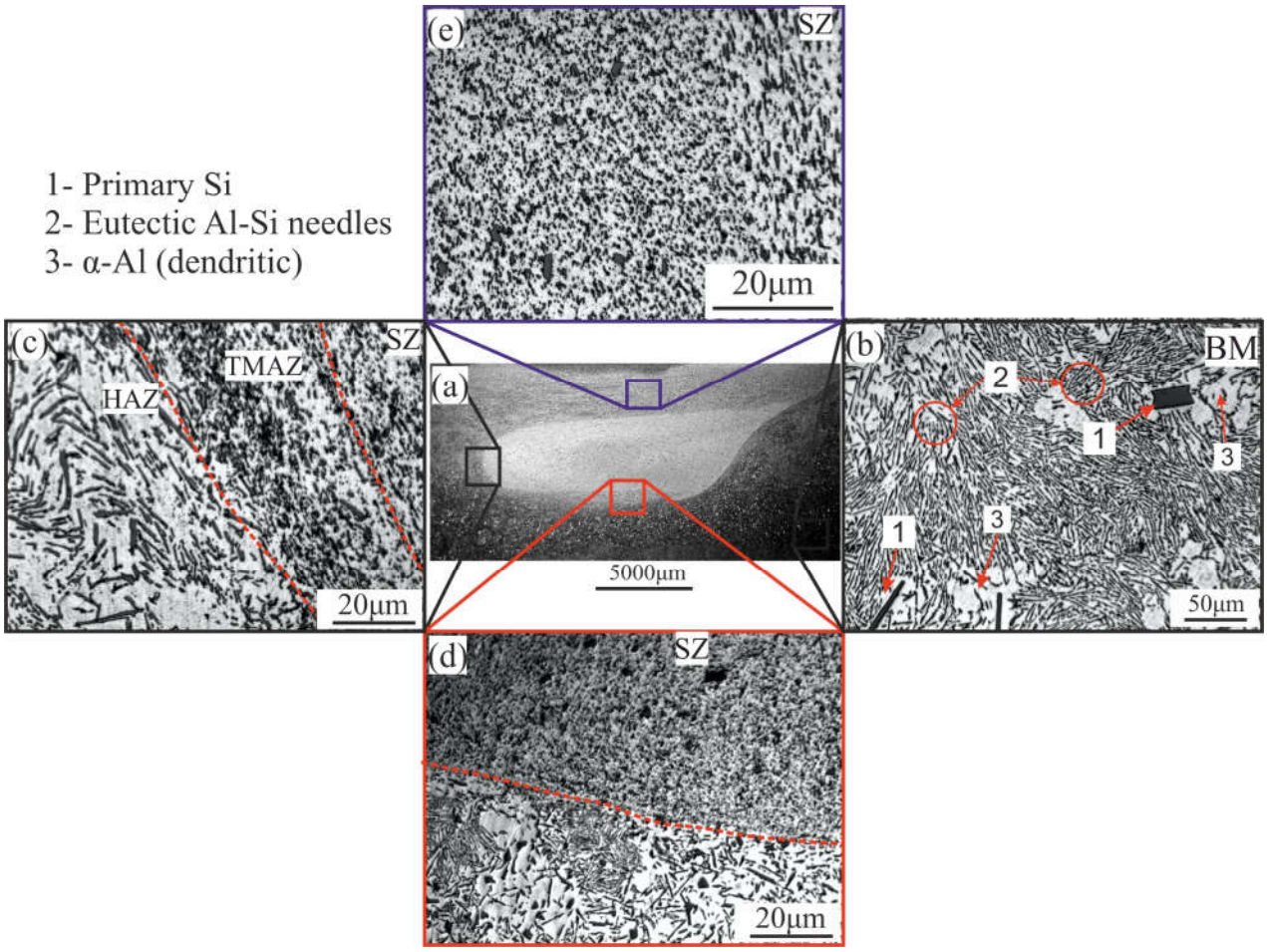

Figure 3. Macro-/micro-graph of Friction Stir Processed sample processed at a rotational speed of 450 rpm and a transverse speed of 20 mm/min using TP tool. (**a**)micro-structure of the processed zone, (**b**) BM area, (**c**) TMAZ and HAZ, (**d**) the bottom of the processed zone, and (**e**) the center of the SZ.

3.2. Hardness

Figure 4 shows the dependence of the hardness of the processed samples on the rotational speed at different traverse speeds, 10, 20, and 40 mm/min. The hardness value of the as-received sheets was 43 ± 3 HV. After FSP using both tools, the hardness was improved significantly at all processing conditions. Figure 5 shows the hardness contour of the processed samples at different feeds (mm/min) and rotational speeds. Figure 5a,b revealed that the obtained hardness was maximum when using both tools at lower rotational speeds and high feed (traverse speed). The TP tool demonstrated higher hardness at lower rotational speed and high feed compared with CP tool. At a lower rotational speed, 350 rpm, for a given rotational speed of the tool, a higher traverse feed rate reduces the time the work material is subjected to friction-generated heat. This inhibits the growth in grains. As the tool's rotating speed increases, the temperature in the stirred zone rises. However, a significant temperature rise results in grain growth, which softens the material.

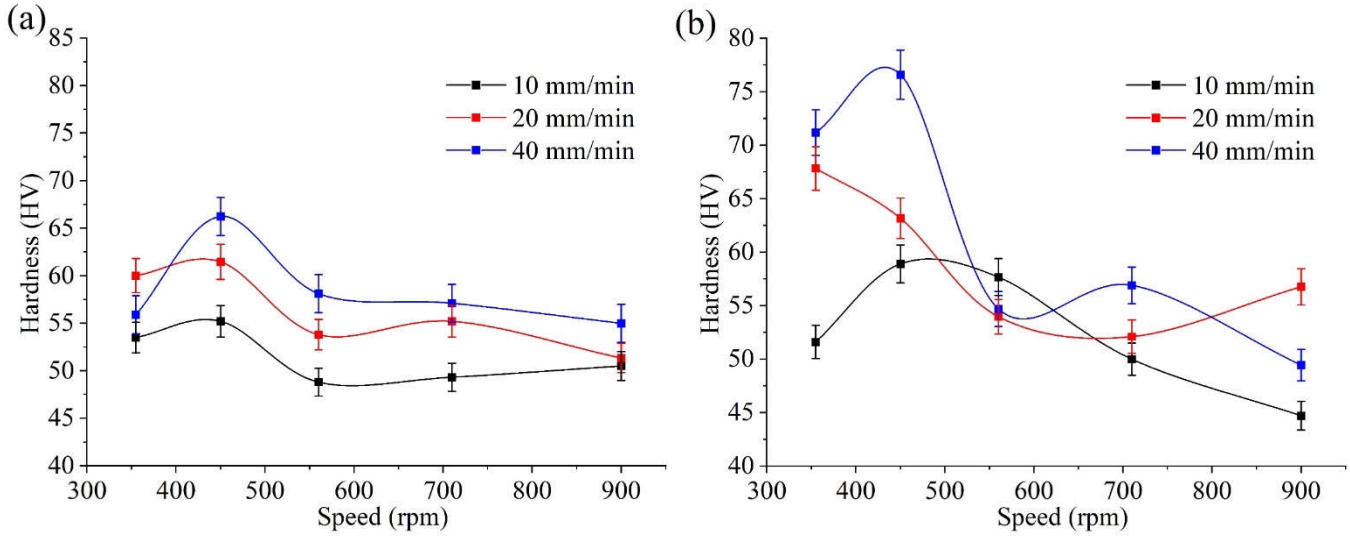

Figure 4. The hardness dependance on rotational speed (rpm) at different traverse speed using (**a**) CP tool and (**b**) TP tool.

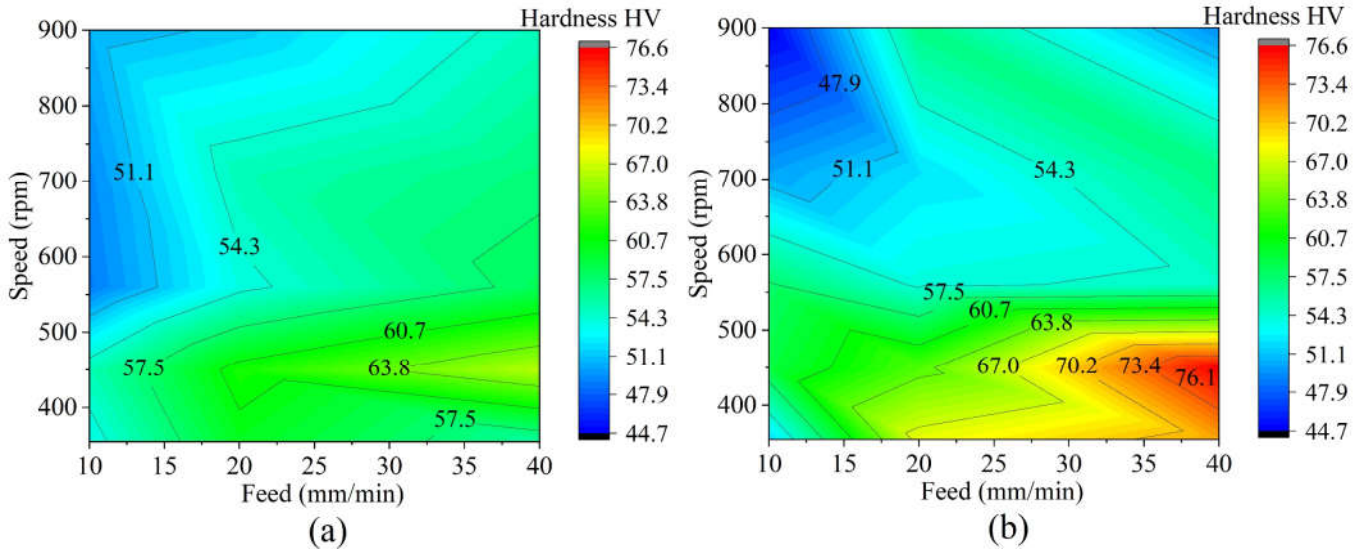

Figure 5. The hardness contour dependence on feed and rotational speed using (**a**) CP tool and (**b**) TP tool.

3.3. Wear Behavior

Figure 6 shows the wear rate contour dependence on the feed (traverse speed) and rotational speed of the samples processed by tools TP and CP. Generally, the as-cast AlSi7Mg0.2 alloy provided a wear rate of 2.41 ± 0.25 g/cm^2. After FSP, the wear rate significantly decreases due to the microstructure modification, refining in eutectic Si- needles and primary Si, and distribution of the refined Si- needles and primary Si in the Al matrix. At high rotational speed and low feed, the frictional heat is high, and the time is enough for grain growth, resulting in a softening structure and a high wear rate. The wear results are consistent with the hardness results—a high harnesses corresponds to a low wear rate.

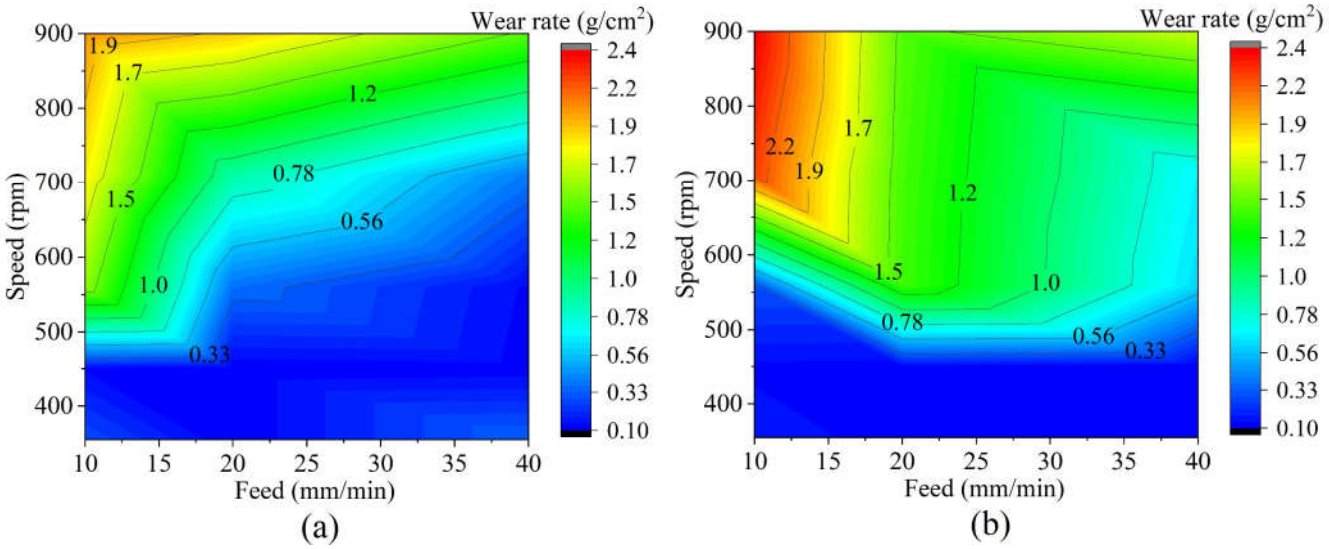

Figure 6. The wear rate contour dependence on feed and rotational speed using (**a**) CP tool and (**b**) TP tool.

Figure 7 shows the SEM micrographs of the worn surface of the samples at rotational speeds of 450 and 900 rpm and traverse speeds of 10 and 40 mm/min using tool TP. Figure 8 reveals that high traverse speed or low tool rotational speed resulted in reduced crack widths and grooves (less damaged and smoother surfaces) than those of high rotational speed and lower feed on the worn surfaces of FSPed zones (Figure 7b). Delamination and deep grooves on the worn surfaces, coupled with plastic deformation at the groove edge, can be observed in the FS-processed sample at 10 mm/min and 900 rpm (Figure 7c). In the case of 10 mm/min compared to 40 mm/min for the same rotational speed, 450 rpm, the delamination and deep grooves on the worn surfaces were heavier (Figure 7a,b). This revealed an improvement in wear rate at low rotational and high traverse speeds. The lack of coarse dendrites throughout the Al alloy and the homogeneous distribution of small Si particles could have reduced friction between the rotating disc and the pin, leading to a lower wear rate at lower rotational speeds. When the rotating speed was high and the traverse speed was low, the amount of heat generated was sufficient for grain growth, leading to higher friction and wear rate. Thus, large deep grooves and delimitations were observed at high rotational speeds (Figure 7c,d)

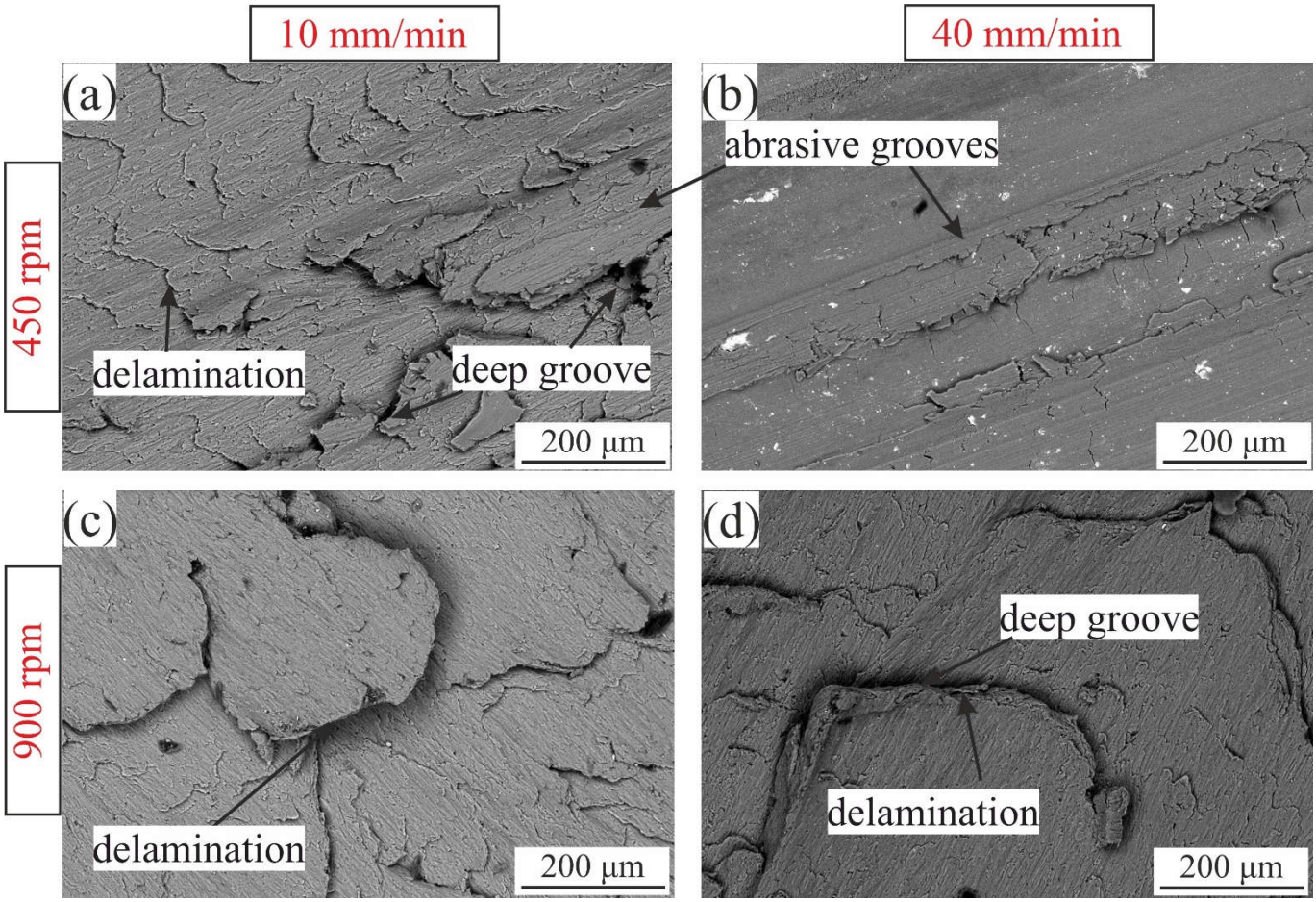

Figure 7. SEM micrograph with a magnification of 500X of the worn surface of FSP samples using TP at rotational speeds of (**a**,**b**) 400 rpm and (**c**,**d**) 900 rpm and transverse speeds of (**a**,**c**) 10 mm/min and (**b**,**d**) 40 mm/min.

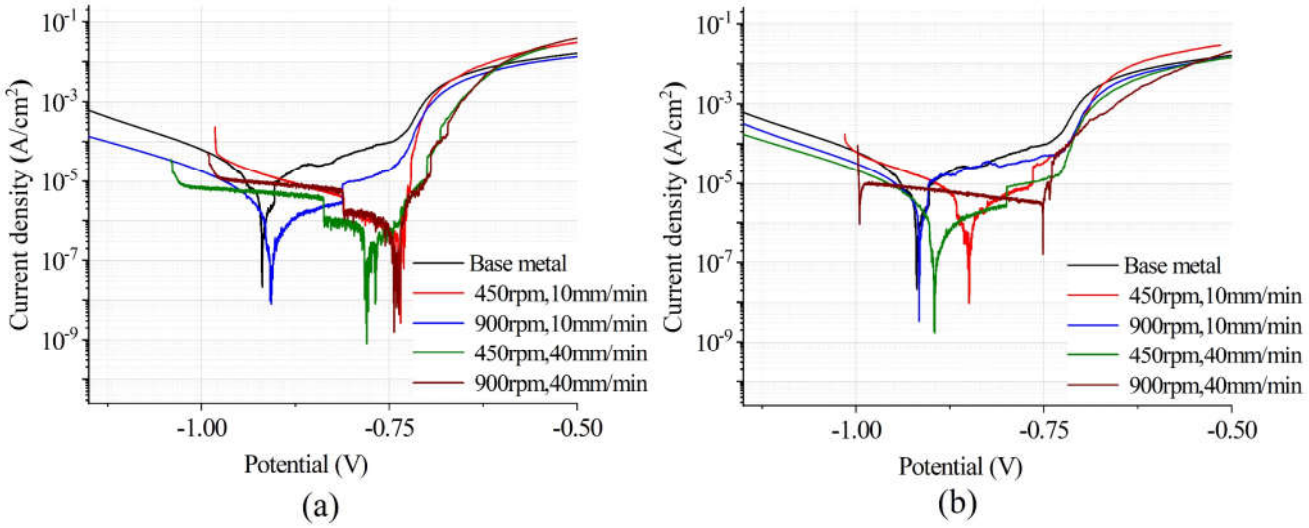

Figure 8. Potentiodynamic polarization plots of the base alloy and the FSP samples at different rotational speeds and traverse speeds using (**a**) CP and (**b**) TP tools.

3.4. Corrosion Behavior

Figure 8 shows the potentiodynamic polarization plots of the base metal alloy and friction-stirred samples at rotational speeds of 450 and 900 and traverse speeds of 10 and 40

mm/min using the TP tool. The microstructure, grain size, and uniformity of the Si particles play a role in the corrosion potential, which differs from one FSPed specimen to another (Figure 8). The base metal has a corrosion potential of around −0.92. That being the case, the base metal is always more reactive than the FSPed samples, evidence that FSP improves corrosion resistance over the base metal samples. Grain refinement during Friction Stir Processing, which distributes the silicon-rich eutectics uniformly in the aluminum matrix, may be responsible for the improved corrosion resistance.

Figure 9 shows the corrosion rate contour dependence on the feed (traverse speed) and rotational speed of the samples processed by tools TP and CP. In the studied range of the traverse speed utilizing both tools, there is no significant difference in the corrosion rate at lower rotational speeds. In contrast, the CP tool showed a higher corrosion rate at an increased rotational speed than the TP tool. The corrosion rate in the base metal was 0.02329 mm/year, which is higher than that of the friction-stirred samples. The decrease in the Si-particles' mean size/aspect ratio and SZ's grain size could cause corrosion resistance improvement at lower rotational speeds. The corrosion resistance of the surface of a metal can be improved to varying degrees by friction stir surface processing (FSP). This is because FSP can refine the grain size of the surface material, creating a more protective oxide layer [42]. The extent of the improvement in corrosion resistance depends on several factors, including the processing parameters and the base metal. High-speed Friction Stir Processing effectively improved the corrosion resistance of the FSPed alloy; hence, the results were consistent with [43].

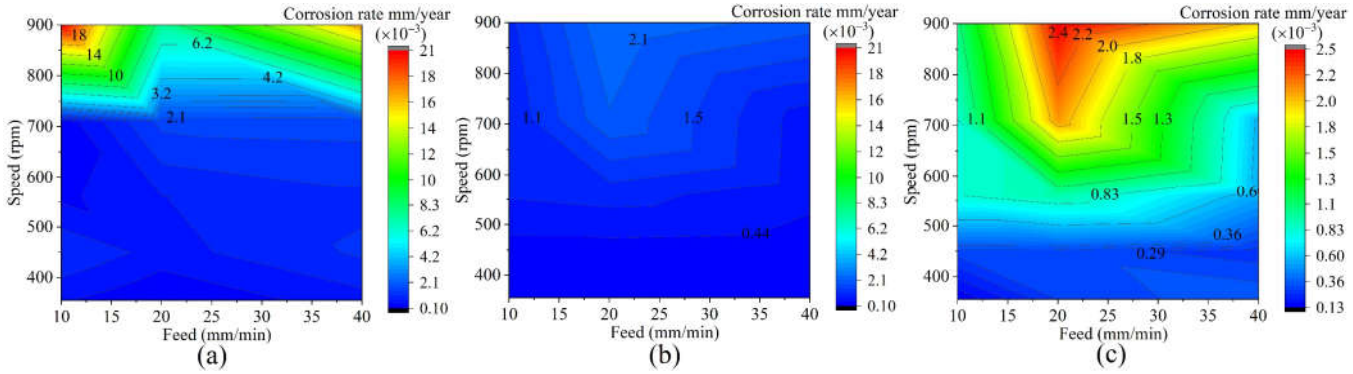

Figure 9. The corrosion rate contour dependence on feed and rotational speed using (**a**) CP tool and (**b**,**c**) TP tools.

3.5. Numerical Simulation

A coupled Eulerian–Lagrangian approach was used to simulate the movement of the material and heat transfer through the workpiece during the process. The workpiece was modeled using the Eulerian approach, while the tool was modeled using the Lagrangian approach. This allowed for a more accurate and effective simulation of the complex thermo-mechanical processes involved. In this section, the numerical fitting of the wear rate (WR), corrosion rate (CR), and average hardness (H) are carried out using both CP and TP profiles. The aim is to establish a comprehensive understanding of the relationship between the FSP process parameters and output variables, thereby enabling the optimization of FSP parameters.

The experimental study conducted involving the variation of rotational speeds and feed rate for both CP and TP was used. The rotational speeds considered were 355, 450, 560, 710, and 900 rpm, while the feed rates included were 10, 20, and 40 mm/min. For each combination of rotational and traverse speeds, the experimental measurements of WR, CR, and H were used in the fitting process, ensuring reliable and accurate data for subsequent analysis.

The output variables were fitted using the thin-plate spline method to predict the output variables. The thin-plate spline method is a popular mathematical technique used for

surface modeling and data fitting. It involves fitting a smooth and continuous surface to input/output data using thin-plate splines, which can provide accurate predictions even for inputs outside the data range. Figures 10 and 11 show the fitted surfaces for the output variables for both CP and TP profiles. All fitted surfaces had an R^2 value of 1, which indicates a perfect fit with the output variables and process parameters.

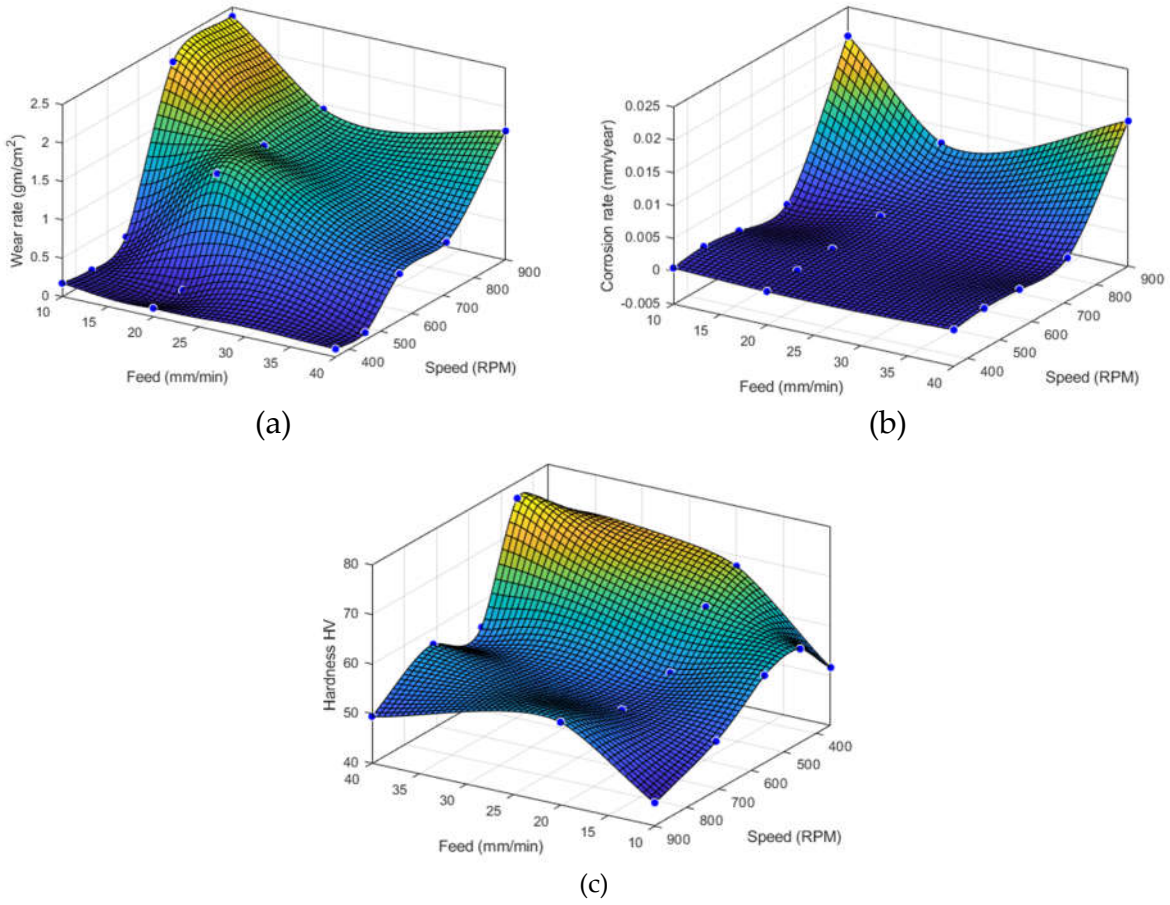

Figure 10. Fitted thin-plate spine surface for CP profile: (**a**) wear rate, (**b**) corrosion rate, (**c**) hardness.

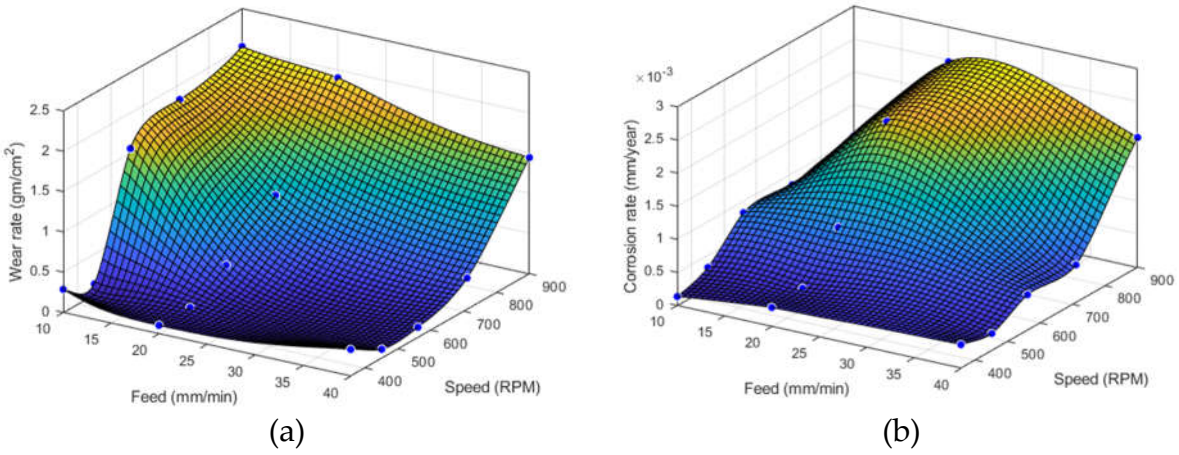

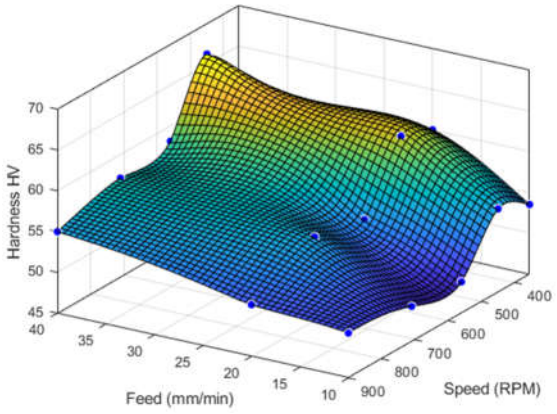

(c)

Figure 11. Fitted thin-plate spine surface for TP profile: (**a**) wear rate (**b**) corrosion rate (**c**) hardness.

In order to determine the optimal speed and feed values that minimize the wear rate and corrosion rate while maximizing the average hardness value, a multi-objective optimization routine was carried out using MATLAB's $f_{minimax}$ function as follows Equation (2)

$$\min(\max(10^4 \times \mathrm{WR}, 100 \times \mathrm{CR}, -\mathrm{H})) \quad (2)$$

The corrosion rate was given a higher weight of 10^4, while the wear rate was given a lower weight of 100, and the hardness was given a negative weight of −1. This ensures that each objective's magnitude does not dominate the optimization process. Using this function, the minimum value of the maximum of the objective functions was calculated for different speed and feed values. The optimization results yielded an optimal feed speed of 19.5 mm/min and a rotational speed of 398.65 rpm for the CP profile. As for the TP, an optimal feed speed of 12 mm/min and a rotational speed of 421.8 rpm were obtained. These optimized values reflect the balance between the minimization of the wear and corrosion rate, as well as the maximization of the hardness value, based on their respective weights. Therefore, this process can be used as a guide to optimize process parameters for the two different tools to ensure the best possible outcomes in terms of the properties of the final product.

3.6. FEA Simulation

The objective of the FE simulation is to create a fitting model to predict the temperature distribution along the workpiece during the dwelling stage as a function of time (t), location from distance from the tool (x), and speed (ω). Various speeds were used in the simulation (450, 600, 800, 900, 1000, 1100, and 1200 rpm) to plot the temperature distribution when the tool dwells up to 5 s. An explicit thermo-mechanical analysis was conducted to accurately and effectively simulate complex thermo-mechanical processes. Furthermore, a coupled Eulerian–Lagrangian approach was utilized to simulate the movement of the material and heat transfer through the workpiece during the process by modeling the workpiece using the Eulerian approach and the Lagrangian approach for the tool, as shown in Figure 12. This approach allows for a more accurate simulation of the complex deformation and flow of the material during the Friction Stir Processing.

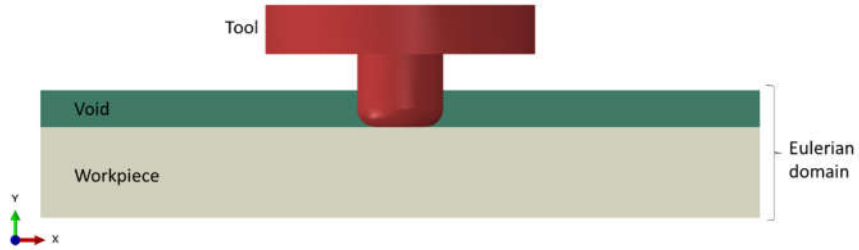

Figure 12. FE model showing the tool (Lagrangian) and the workpiece (Eulerian domain).

Moreover, the tool was modeled as a rigid, straight cylindrical shape to simplify and improve the computational efficiency of the simulation. The tool pin has a diameter of 4.8 mm and a length of 4 mm, while the shoulder has a diameter of 15 mm and a thickness of 2.7 mm. The alloy was modeled using the Johnson–Cook material model shown below Equations (3) and (4):

$$\sigma = \left[A + B\left(\bar{\varepsilon}_{pl}\right)^{n}\right]\left(1 - \hat{\theta}^{m}\right) \tag{3}$$

$$\hat{\theta} = \begin{cases} 0 & \text{for } \theta < \theta_{room} \\ \dfrac{(\theta - \theta_{room})}{(\theta_{melt} - \theta_{room})} & \text{for } \theta_{room} \le \theta \le \theta_{melt} \\ 1 & \text{for } \theta > \theta_{melt} \end{cases} \tag{4}$$

where A = 224 Mpa is the initial yield strength of the material, B = 670 Mpa is the strain hardening stress coefficient, n = 0.14 is the strain hardening exponent, m = 0.02 is the thermal softening coefficient, θ is the material temperature, θ_{melt} = 656 °C is the melting temperature, θ_{room} is the room temperature, and $\bar{\varepsilon}_{pl}$ is the plastic strain. These parameters were obtained experimentally. The model was simplified by excluding the dependence on strain rate.

The Eulerian domain was set to be 40 × 40 × 7 mm^3, with the workpiece filling up to 5 mm of the domain thickness, as shown in Figure 12. At the welding location, where the tool makes contact with the workpiece, Eulerian elements of size 0.5 mm were generated. In contrast, the regions further away from the workpiece used elements of a larger size, as shown in Figure 13. The total number of elements generated was 35,000. The workpiece was fixed from two sides (sides A and B, as shown in Figure 13), and the initial temperature was set to 25 °C. Additionally, a convection boundary condition was specified over the workpiece with an ambient temperature of 25 °C and a convection coefficient of 2.5 w/m^2-k. This boundary condition represents the cooling effect of the surrounding air on the workpiece during the process.

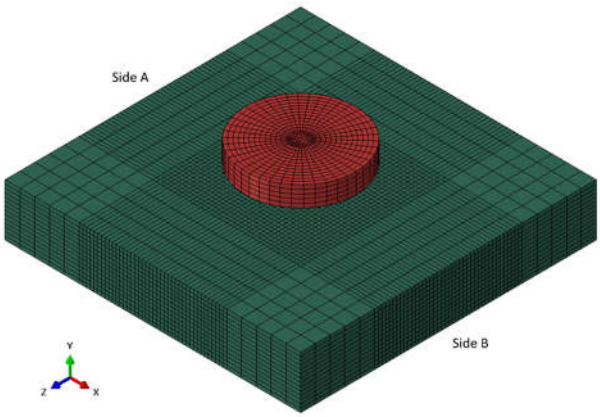

Figure 13. Generated FE mesh of the workpiece and tool.

Figure 14 shows the temperature contour plot on the workpiece after the tool has dwelled for 5 s. To analyze the temperature distribution in the workpiece, the temperature profile along the red line shown in the figure was plotted for the speeds mentioned, as shown in Figure 15. The maximum temperature near the tool side reached approximately 280 °C and 590 °C for 450 and 1200 rpm, respectively, when the tool dwelled for 5 s.

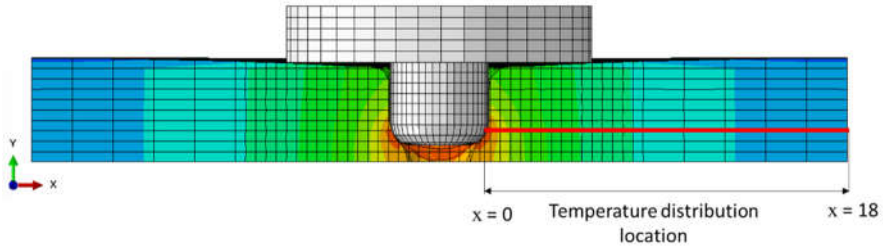

Figure 14. Temperature contour plot in the workpiece when the tool dwelled for 5 s.

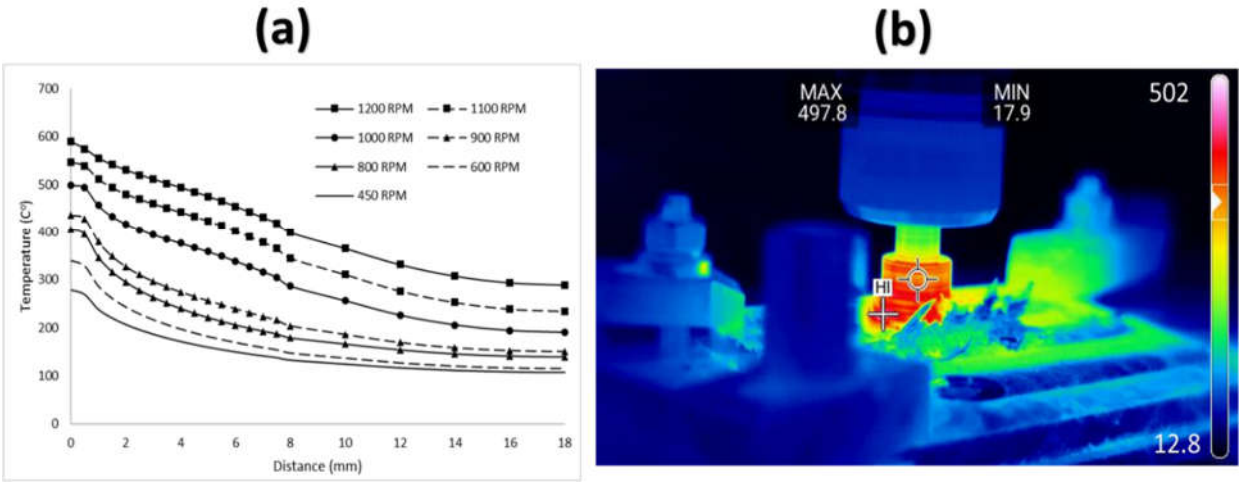

Figure 15. Temperature distribution along the workpiece: (**a**) prediction model, (**b**) typical thermal image at 900 rpm tool rotation speed with 40 mm/min traverse speed.

In order to find a suitable function for the fitting process, the temperature variation with the process parameter was investigated. Upon analyzing the temperature graphs, the variation of temperature along the workpiece at different speeds was found to resemble a sigmoidal function, indicative of a gradual increase in temperature followed by a plateau. Furthermore, the correlation between the temperature and the rotational speed demonstrated a quadratic relationship, implying that the temperature increased more rapidly with higher rotational speeds. This behavior was consistent when observing the temperature variation concerning time, especially near the tool side (Figures 16 and 17).

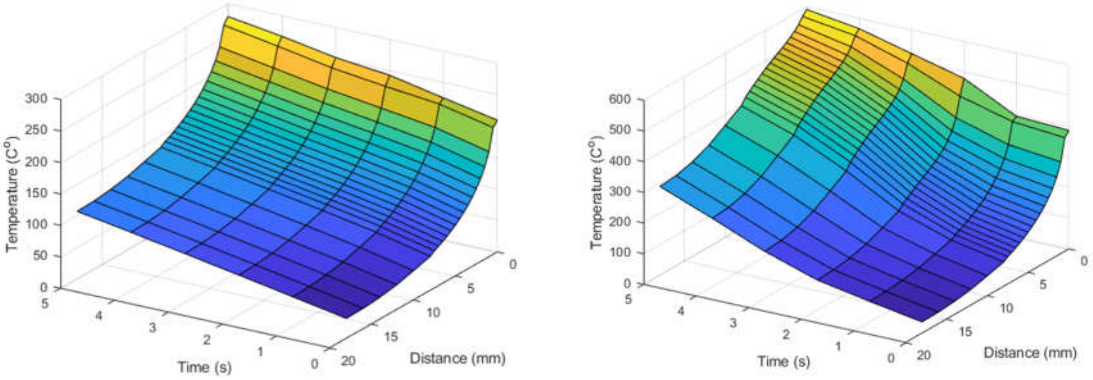

Figure 16. Temperature distribution as a function of time and distance at (**a**) 450 rpm and (**b**) 1200 rpm.

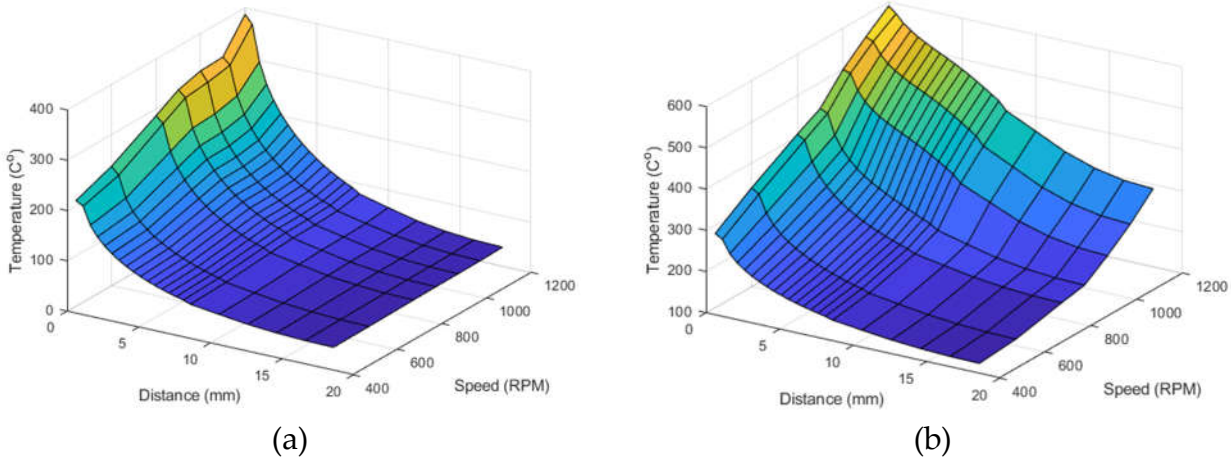

Figure 17. Temperature distribution as a function of time and speed at (**a**) 0 s and (**b**) 5 s.

Based on the previous results, MATLAB was used to develop the fitting function below to describe the modeled behavior of the workpiece temperature Equation (5).

$$f(\omega, x, t) = -107.92 + \left(\frac{105.2311}{\left[1 + \left(\frac{x}{1.0411}\right)^2\right]^{0.13998}}\right)(2.3786 - 0.0019\omega)(35.341 + 3.3532t + 0.41596t^2) \quad (5)$$

The fitted function had an R-squared value of 0.934 with an RMS of 30, signifying a good fit and allowing for further analysis of the model's accuracy. After obtaining the fitting function, key parameters of the model were determined, enabling a more detailed understanding of the relationship between processing parameters and temperature development during the Friction Stir Processing. These findings are essential in achieving optimized process parameters for high-quality welds with minimal defects and distortions. By utilizing the information derived from the simulation, future research can focus on refining the model and tailoring the Friction Stir Processing parameters to specific material properties and requirements.

4. Conclusions

This study investigated the effect of Friction Stir Processing (FSP) parameters on the microstructure, hardness, corrosion, and wear resistance of A356 alloy.

- The results showed that the FSP parameters, such as rotational speed, traverse speed, and tool geometry, had a significant impact on the microstructure and mechanical properties of the alloy. The FSPed samples had a finer grain size than the as-received alloy. This was attributed to the intense plastic deformation and dynamic recrystallization that occurred during FSP. The finer grain size resulted in a number of improvements, including:
- The hardness of the FSPed samples was increased by up to 50% compared to the as-received alloy. This was due to the increased dislocation density and grain boundary strengthening;
- The FSPed samples' wear rate decreased by up to 60% compared to the as-received alloy. This was attributed to the smoother surface and the increased hardness of the FSPed samples;
- The corrosion resistance of the FSPed samples was also improved. This was attributed to the finer grain size, resulting in a more uniform Si-particle distribution;
- The temperature distribution results during Friction Stir Processing (FSP) using finite element simulation were highly dependent on the process parameters, such as the rotational speed and the dwell time;
- The results of this study can be used to develop a fitting model to predict the temperature distribution along the workpiece during the dwelling stage. This model can be used to optimize the process parameters for different applications, such as achieving a desired temperature distribution or minimizing the risk of defects.

Author Contributions: Conceptualization, G.A.; Methodology, S.S.M., E.B.M. and A.O.M.; Software, M.A.A.; Formal analysis, A.O.M.; Investigation, A.O.M. and S.S.M.; Data curation, M.A.A. and G.A.; Writing—original draft, E.B.M.; Writing—review & editing, A.O.M.; Visualization, G.A. All authors have read and agreed to the published version of the manuscript.

Funding: This research work was funded by Institutional Fund Projects under grant no. (IFPIP:606-135-1443). The authors gratefully acknowledge the technical and financial support provided by the Ministry of Education and King Abdulaziz University, DSR, Jeddah, Saudi Arabia.

Institutional Review Board Statement: Not applicable

Informed Consent Statement: Not applicable

Data Availability Statement: Not applicable.

Conflicts of Interest: The authors declare no conflict of interest.

Nomenclature

FSP	Friction Stir Processing
SDAS	Secondary dendrite arm spacing
CNC	Computer numerical control
TP	Triangular pin with cylindrical corners pin tool
OM	Optical microscope
ΔW	weight loss (g)
SCE	Saturated calomel electrode
BM	Base metal, non-affected zone
FEA	Finite elements analysis
TMAZ	Thermomechanical affected zone
WR	Wear rate, g/cm^2
H	Hardness
CEL	Coupled Eulerian–Lagrangian
SLM	Selective laser melting
CP	Cylindrical pin profiled tool

rpm	Tool rotational speeds, revolution per minute
SEM	Scanning electron microscope
A	Area of exposed surface to the friction (cm^2)
Rp	Resistance polarization
HAZ	Heat-affected zone
SZ	Stirred or nugget zone
CR	Corrosion rate

References

1. Sun, H.; Yang, S.; Jin, D. Improvement of Microstructure, Mechanical Properties and Corrosion Resistance of Cast Al–12Si Alloy by Friction Stir Processing. *Trans. Indian Inst. Met.* **2018**, *71*, 985–991.
2. Ma, Z.Y.; Sharma, S.R.; Mishra, R.S. Microstructural modification of as-cast Al-Si-Mg alloy by friction stir processing. *Metall. Mater. Trans. A* **2006**, *37*, 3323–3336.
3. Moustafa, E.B.; Taha, M.A. The Effect of Mono and Hybrid Additives of Ceramic Nanoparticles on the Tribological Behavior and Mechanical Characteristics of an Al-Based Composite Matrix Produced by Friction Stir Processing. *Nanomaterials* **2023**, *13*, 2148. https://doi.org/10.3390/nano13142148.
4. Ahmed, H.M.; Ahmed, H.A.; Hefni, M.; Moustafa, E.B. Effect of Grain Refinement on the Dynamic, Mechanical Properties, and Corrosion Behaviour of Al-Mg Alloy. *Metals* **2021**, *11*, 1825. https://doi.org/10.3390/met11111825.
5. Ma, Z.Y.; Pilchak, A.L.; Juhas, M.C.; Williams, J.C. Microstructural refinement and property enhancement of cast light alloys via friction stir processing. *Scr. Mater.* **2008**, *58*, 361–366.
6. Ma, Z.Y. Friction Stir Processing Technology: A Review. *Metall. Mater. Trans. A* **2008**, *39*, 642–658.
7. Ahmed, S.; Malik, M.V.; Ahmad, B. Surface moderation and composite fabrication of die-cast magnesium alloys via friction stir processing: A review. *Adv. Mater. Process. Technol.* **2022**, *8*, 3635–3655.
8. Wang, F.; Zheng, R.; Chen, J.; Lyu, S.; Li, Y.; Xiao, W.; Ma, C. Significant improvement in the strength of Mg-Al-Zn-Ca-Mn extruded alloy by tailoring the initial microstructure. *Vacuum* **2019**, *161*, 429–433.
9. Moustafa, E. Effect of Multi-Pass Friction Stir Processing on Mechanical Properties for AA2024/Al_2O_3 Nanocomposites. *Materials* **2017**, *10*, 1053. https://doi.org/10.3390/ma10091053.
10. Moustafa, E.B.; Abushanab, W.S.; Melaibari, A.; Mikhaylovskaya, A.V.; Abdel-Wahab, M.S.; Mosleh, A.O. Nano-Surface Composite Coating Reinforced by Ta_2C, Al_2O_3 and MWCNTs Nanoparticles for Aluminum Base via FSP. *Coatings* **2021**, *11*, 1496.
11. Alidokht, S.A.; Abdollah-Zadeh, A.; Soleymani, S.; Assadi, H. microstructure and tribological performance of an aluminium alloy based hybrid composite produced by friction stir processing. *Mater. Des.* **2011**, *32*, 2727–2733.
12. El-Mahallawy, N.A.; Zoalfakar, S.H.; Maboud, A.A.G.A. Microstructure investigation, mechanical properties and wear behavior of Al 1050/SiC composites fabricated by friction stir processing (FSP). *Mater. Res. Express* **2019**, *6*, 096522.
13. Madhusudhan Reddy, G.; Srinivasa Rao, K. Enhancement of wear and corrosion resistance of cast A356 aluminium alloy using friction stir processing. *Trans. Indian Inst. Met.* **2010**, *63*, 793–798.
14. Rao, A.G.; Katkar, V.A.; Gunasekaran, G.; Deshmukh, V.P.; Prabhu, N.; Kashyap, B.P. Effect of multipass friction stir processing on corrosion resistance of hypereutectic Al–30Si alloy. *Corros. Sci.* **2014**, *83*, 198–208.
15. Yang, T.; Wang, K.; Wang, W.; Peng, P.; Huang, L.; Qiao, K.E.; Jin, Y. Effect of Friction Stir Processing on Microstructure and Mechanical Properties of $AlSi_{10}Mg$ Aluminum Alloy Produced by Selective Laser Melting. *JOM* **2019**, *71*, 1737–1747.
16. Macías, J.G.S.; Elangeswaran, C.; Zhao, L.; Van Hooreweder, B.; Adrien, J.; Maire, E.; Buffière, J.-Y.; Ludwig, W.; Jacques, P.J.; Simar, A. Ductilisation and fatigue life enhancement of selective laser melted $AlSi_{10}Mg$ by friction stir processing. *Scr. Mater.* **2019**, *170*, 124–128.
17. Cabrini, M.; Lorenzi, S.; Pastore, T.; Pellegrini, S.; Ambrosio, E.P.; Calignano, F.; Manfredi, D.; Pavese, M.; Fino, P. Effect of heat treatment on corrosion resistance of DMLS $AlSi_{10}Mg$ alloy. *Electrochim. Acta* **2016**, *206*, 346–355.
18. Pisarek, B.P.; Rapiejko, C.; Szymczak, T.; Pacyniak, T. Effect of Alloy Additions on the Structure and Mechanical Properties of the $AlSi_7Mg_{0.3}$ Alloy. *Arch. Foundry Eng.* **2017**, *17*, 137–142.
19. Babu, S.S.; Livingston, J.; Lippold, J.C. Physical Simulation of Deformation and Microstructure Evolution During Friction Stir Processing of Ti-6Al-4V Alloy. *Metall. Mater. Trans. A* **2013**, *44*, 3577–3591.
20. Teo, G.S.; Liew, K.W.; Kok, C.K. Optimization of Friction Stir Processing Parameters of Recycled AA 6063 for Enhanced Surface Microhardness and Tribological Properties. *Metals* **2022**, *12*, 310. https://doi.org/10.3390/met12020310.
21. Liew, K.W.; Chung, Y.Z.; Teo, G.S.; Kok, C.K. Effect of Tool Pin Geometry on the Microhardness and Surface Roughness of Friction Stir Processed Recycled AA 6063. *Metals* **2021**, *11*, 1695. https://doi.org/10.3390/met11111695.
22. Ghosh, M.; Kumar, K.; Kailas, S.V.; Ray, A.K. Optimization of friction stir welding parameters for dissimilar aluminum alloys. *Mater. Des.* **2010**, *31*, 3033–3037.
23. Vaira Vignesh, R.; Padmanaban, R. Influence of friction stir processing parameters on the wear resistance of aluminium alloy AA5083. *Mater. Today Proc.* **2018**, *5 Pt 2*, 7437–7446.

24. Ai, Y.; Yu, L.; Huang, Y.; Liu, X. The investigation of molten pool dynamic behaviors during the "∞" shaped oscillating laser welding of aluminum alloy. *Int. J. Therm. Sci.* **2022**, *173*, 107350.
25. Rathee, S.; Maheshwari, S.; Siddiquee, A.N.; Srivastava, M.; Sharma, S.K. Process parameters optimization for enhanced microhardness of AA 6061/ SiC surface composites fabricated via Friction Stir Processing (FSP). *Mater. Today: Proc.* **2016**, *3 Pt B*, 4151–4156.
26. Ansari, M.A.; Samanta, A.; Behnagh, R.A.; Ding, H. An efficient coupled Eulerian-Lagrangian finite element model for friction stir processing. *Int. J. Adv. Manuf. Technol.* **2019**, *101*, 1495–1508.
27. Tutunchilar, S.; Haghpanahi, M.; Givi, M.B.; Asadi, P.; Bahemmat, P. Simulation of material flow in friction stir processing of a cast Al–Si alloy. *Mater. Des.* **2012**, *40*, 415–426.
28. Ai, Y.; Liu, X.; Huang, Y.; Yu, L. Numerical analysis of the influence of molten pool instability on the weld formation during the high speed fiber laser welding. *Int. J. Heat Mass Transf.* **2020**, *160*, 120103.
29. Ji, S.D.; Shi, Q.Y.; Zhang, L.G.; Zou, A.L.; Gao, S.S.; Zan, L.V. Numerical simulation of material flow behavior of friction stir welding influenced by rotational tool geometry. *Comput. Mater. Sci.* **2012**, *63*, 218–226.
30. Aljoaba, S.Z.; Jawahir, I.S.; Dillon, O.W.; Ali, M.H.; Khraisheh, M.K. Modeling of friction stir processing using 3D CFD analysis. *Int. J. Mater. Form.* **2009**, *2*, 315.
31. Zhang, C.; Huang, G.; Cao, Y.; Zhu, Y.; Liu, Q. On the microstructure and mechanical properties of similar and dissimilar AA7075 and AA2024 friction stir welding joints: Effect of rotational speed. *J. Manuf. Process.* **2019**, *37*, 470–487.
32. Rezaei, H.; Mirbeik, M.H.; Bisadi, H. Effect of rotational speeds on microstructure and mechanical properties of friction stir-welded 7075-T6 aluminium alloy. *Proc. Inst. Mech. Eng. Part C J. Mech. Eng. Sci.* **2011**, *225*, 1761–1773.
33. Behnagh, R.A.; Givi, M.K.B.; Akbari, M. Mechanical Properties, Corrosion Resistance, and Microstructural Changes during Friction Stir Processing of 5083 Aluminum Rolled Plates. *Mater. Manuf. Process.* **2012**, *27*, 636–640.
34. Jana, S.; Mishra, R.S.; Baumann, J.A.; Grant, G.J. Effect of Friction Stir Processing on Microstructure and Tensile Properties of an Investment Cast Al-7Si-0.6Mg Alloy. *Metall. Mater. Trans. A* **2010**, *41*, 2507–2521.
35. Zahmatkesh, B.; Enayati, M.H.; Karimzadeh, F. Tribological and microstructural evaluation of friction stir processed Al2024 alloy. *Mater. Des.* **2010**, *31*, 4891–4896.
36. Moeini, G.; Sajadifar, S.V.; Engler, T.; Heider, B.; Niendorf, T.; Oechsner, M.; Böhm, S. Effect of Friction Stir Processing on Microstructural, Mechanical, and Corrosion Properties of Al-Si12 Additive Manufactured Components. *Metals* **2020**, *10*, 85. https://doi.org/10.3390/met10010085.
37. García-Bernal, M.A.; Mishra, R.S.; Verma, R.; Hernández-Silva, D. Influence of friction stir processing tool design on microstructure and superplastic behavior of Al-Mg alloys. *Mater. Sci. Eng. A* **2016**, *670*, 9–16.
38. Surekha, K.; Murty, B.S.; Rao, K.P. Effect of processing parameters on the corrosion behaviour of friction stir processed AA 2219 aluminum alloy. *Solid State Sci.* **2009**, *11*, 907–917.
39. García-Bernal, M.A.; Mishra, R.S.; Verma, R.; Hernández-Silva, D. Enhancing the corrosion properties of additively manufactured AlSi10Mg using friction stir processing. *Corros. Sci.* **2021**, *178*, 109073.
40. *ASTM E384-17*; Standard Test Method for Microindentation Hardness of Materials. Available online: https://www.astm.org/e0384-17.html (accessed on 5 August 2023).
41. *ASTM G99-04*; Standard Test Method for Wear Testing with a Pin-on-Disk Apparatus. Available online: https://www.astm.org/g0099-04.html (accessed on 5 August 2023).
42. Ge, X.; Song, W.; Jiang, D.; Cao, S.; Wang, H.; Liu, S. Study on the Corrosion Resistance of the H65 Copper Alloy Surface Modified by Friction Stir Surface Processing. *Int. J. Electrochem. Sci.* **2022**, *17*, 22061.
43. Liu, F.; Ji, Y.; Sun, Z.; Liu, J.; Bai, Y.; Shen, Z. Enhancing corrosion resistance and mechanical properties of AZ31 magnesium alloy by friction stir processing with the same speed ratio. *J. Alloys Compd.* **2020**, *829*, 154452.